





Effect of curvature on the eigenstates of magnetic skyrmions

Anastasiia Korniienko ^{1,2}, Attila Kákay ², Denis D. Sheka ³, and Volodymyr P. Kravchuk ^{4,5,*}

¹*Department of Physics, Technical University of Munich, 85748 Garching, Germany*

²*Helmholtz-Zentrum Dresden-Rossendorf e.V., Institute of Ion Beam Physics and Materials Research, 01328 Dresden, Germany*

³*Taras Shevchenko National University of Kyiv, 01601 Kyiv, Ukraine*

⁴*Institut für Theoretische Festkörperphysik, Karlsruher Institut für Technologie, D-76131 Germany*

⁵*Bogolyubov Institute for Theoretical Physics of National Academy of Sciences of Ukraine, 03143 Kyiv, Ukraine*



(Received 9 April 2020; revised 26 June 2020; accepted 30 June 2020; published 20 July 2020)

Spectrum of spin eigenmodes localized on a ferromagnetic skyrmion pinned by a geometrical defect (bump) of magnetic films is studied theoretically. By means of direct numerical solution of the corresponding eigenvalue problem and finite element micromagnetic simulations we demonstrate that the curvature can induce localized modes with higher azimuthal and radial quantum numbers, which are absent for planar skyrmions (for the same parameters). The eigenfrequencies of all modes, except the breathing and gyromodes decreases with increasing curvature. Due to the translational symmetry break, the zero translational mode of the skyrmion gains a finite frequency and forms the gyromode, which describes the uniform rotation of skyrmions around the equilibrium position. To treat the gyromotion analytically we developed a Thiele-like collective variable approach. We show that Néel skyrmions in curvilinear films experience a driving force originating from the gradient of the mean curvature. The gyrofrequency of the pinned skyrmion is proportional to the second derivative of the mean curvature at the point of equilibrium.

DOI: [10.1103/PhysRevB.102.014432](https://doi.org/10.1103/PhysRevB.102.014432)

I. INTRODUCTION

Nowadays, magnetic skyrmions [1–5] are the subject of extensive studies. This can be explained by the fundamental interest in the physics of topological solitons [6], by the feasibility to use single skyrmions as possible bit carriers in various memory and logic devices [4,5,7–14], and also due to the ability to realize skyrmion lattices [15–19] with possible applications in devices relying on the topological Hall effect [20–23].

Introducing curvature by bending magnetic thin film the properties of magnetic skyrmions is changed. The majority of the new effects related to surface curvature can be explained in terms of the effective magnetic interactions caused by locally curved geometries: (i) curvilinear geometry-induced effective anisotropy and (ii) curvilinear geometry-induced effective Dzyaloshinskii-Moriya interaction (DMI) [24–26]. This effective DMI emerges as an antisymmetric part of the common isotropic exchange in a curvilinear frame of reference which follows the surface. The transition into the curvilinear frame of reference is not just a mathematical trick, but is physically conditioned by the presence of the magnetic interactions determined by the film geometry, e.g., the uniaxial anisotropy whose axis follows the surface normal, or intrinsic, DMI of the surface type [27–29]. A convincing example of curvature-induced DMI effect is the stabilization of ferromagnetic skyrmions on a curvilinear shell free of intrinsic DMI [30,31].

Previously it was reported [32] that a local curvature (bump) of the film can create attracting as well as repulsing potentials for skyrmions. In the case of attraction the pinned skyrmion can possess a multiplet of states and the regular arrangement of the bumps will result in an artificial skyrmion lattice as the ground state of the system [32]. These interesting findings can be considered for applications. The present paper is a continuation of the static study presented in Ref. [32] and is focused on the linear dynamics of skyrmions pinned on bumps.

Here, we report on the study of magnon eigenexcitations in ferromagnetic skyrmions pinned on geometrical defects with rotational symmetry. Three different methods are used. (i) We formulate and solve numerically the eigenvalue problem for a skyrmion on a curvilinear bump. This is the generalization of the previously developed analysis in Ref. [33] for the case of planar films. (ii) We perform full-scale finite element micromagnetic simulations using our code TETRAMAG [34]. (iii) We generalize the Thiele equation for the case of a ferromagnetic topological soliton on a curvilinear film. The generalized equation keeps the form of the common Thiele equation but the gyrovector follows the surface normal. The gyrovector amplitude approaches its planar value in the limited case when the skyrmion radius is much smaller as compared to the curvature radii. The curvature-induced driving force proportional to the gradient of the mean curvature appears for the case of Néel skyrmions. This effect takes place due to the curvilinear geometry-induced effective DMI. It is analogous to the curvature-induced domain walls motion in curvilinear wires [35,36]. We utilize the generalized Thiele equation to obtain the analytical expression for the gyromode of a small-radius Néel skyrmion.

*volodymyr.kravchuk@kit.edu

The paper is organized as follows. In Sec. II we introduce the Hamiltonian of the system and discuss the magnetic interactions which are taken into account. In Sec. III we obtain the static solution for a skyrmion on a curvilinear defect of the rotational symmetry (bump) and compare it to the micromagnetic simulations. In Sec. IV we formulate and solve numerically the eigenvalue problem for spin waves excited over the skyrmion pinned on a bump. In Sec. V we utilize the generalized Thiele equation to derive the analytical expression for the gyromode eigenfrequency. In Sec. VI we summarize our results. In Appendix A we list the eigenfunctions of the localized eigenmodes obtained in Sec. IV. In Appendix B we generalize the Thiele equation for the case of a curvilinear shell. In Appendix C we provide details of the micromagnetic simulations.

II. MODEL

The magnetic medium assumed to be a thin film of a chiral ferromagnet with perpendicular easy-axis anisotropy can be modeled by the following energy functional:

$$E = L \int [A\mathcal{E}_x + K_u(1 - m_n^2) + \mathcal{D}\mathcal{E}_D] dS, \quad (1)$$

where L is the film thickness and the integration is performed over the film area. The first term of the integrand is the exchange energy density with $\mathcal{E}_x = \sum_{i=x,y,z} (\partial_i \mathbf{m})^2$, with A being the exchange constant. Here $\mathbf{m} = \mathbf{M}/M_s$ is the unit magnetization vector with M_s being the saturation magnetization. The second term is the easy-normal anisotropy with $K_u > 0$ and $m_n = \mathbf{m} \cdot \mathbf{n}$ is the normal magnetization component with \mathbf{n} being the unit normal to the surface. The exchange-anisotropy competition results in the magnetic length $\ell = \sqrt{A/K_u}$, determining the characteristic lengthscale of the system (on which noncollinear magnetic structures can form). The last term in Eq. (1) represents the Dzyaloshinskii-Moriya interaction with $\mathcal{E}_D = m_n \nabla \cdot \mathbf{m} - \mathbf{m} \cdot \nabla m_n$. Such a kind of DMI originates from the inversion symmetry breaking at the film interface; it is typical for ultrathin films [27–29] or bilayers [37], and can result in formation of Néel (hedgehog) skyrmions [8,38]. The magnetostatic contribution is not included explicitly into our model since, in ultrathin films, it can be reduced as the renormalization of the anisotropy $K_u \rightarrow K_u^{\text{eff}} = K_u - 2\pi M_s^2$ [39–41], leading to an effective anisotropy constant. In Eq. (1) it is assumed that the magnetization profile is uniform along the direction of the normal to the surface. The magnetization dynamics is described by the Landau-Lifshitz-Gilbert equation

$$\partial_t \mathbf{m} = \frac{\gamma_0}{M_s} \left[\mathbf{m} \times \frac{\delta E}{\delta \mathbf{m}} \right] + \eta [\mathbf{m} \times \partial_t \mathbf{m}], \quad (2)$$

where γ_0 is gyromagnetic ratio and η is the Gilbert damping.

Our model system is a magnetic film with a curvilinear defect of rotational symmetry is considered. To this end we describe our film as a surface of revolution $\sigma(s, \chi) = r(s)(\hat{x} \cos \chi + \hat{y} \sin \chi) + z(s)\hat{z}$. Here $\chi \in [0, 2\pi)$ is the azimuthal angle and $s \geq 0$ is the radial distance along the surface. The pair of functions [42] determine the shape of the surface as shown in Fig. 1(d): $r(s)$ and $z(s)$ denote the distance to the point of the surface with coordinate s from the

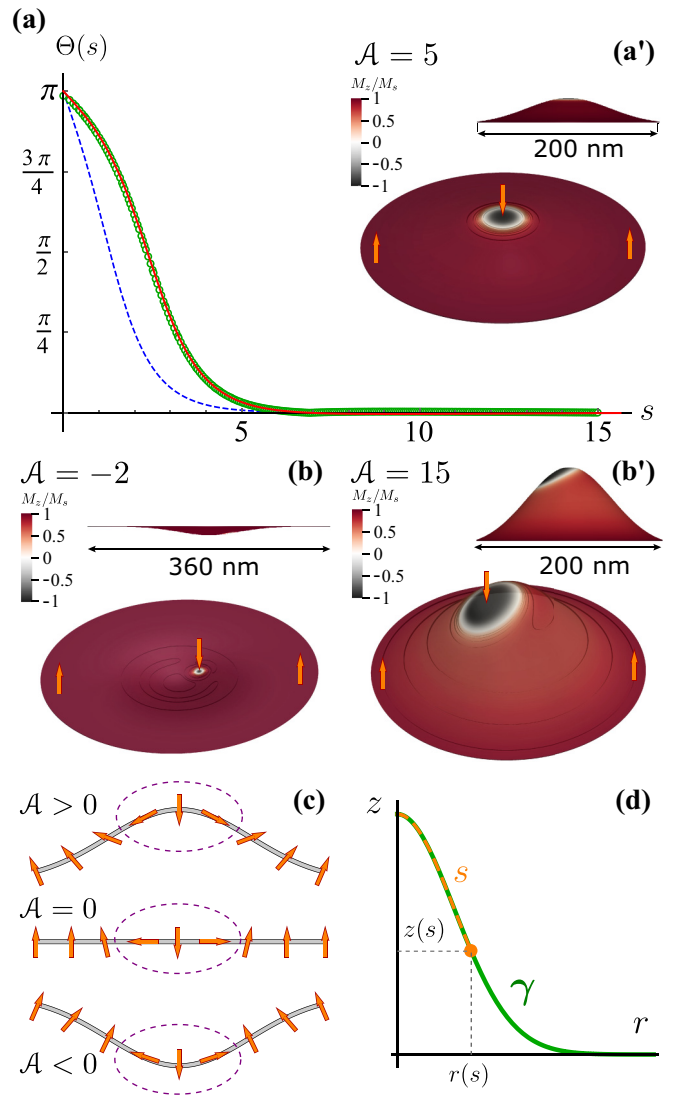


FIG. 1. Skyrmion states of Gaussian bumps (4) obtained for various bump amplitudes $\mathcal{A} = -2, 5, 15$ and fixed width $r_0 = 8$ and dimensionless DMI constant $d = 0.98$. (a) Stable skyrmion profile $\Theta(s)$ obtained for the bump with $\mathcal{A} = 5$ by means of numerical solution of Eq. (3) (solid line) and micromagnetic simulations (green hollow dots) compared to the skyrmion profile on the planar film (dashed line). (a') The magnetization profile obtained from micromagnetic simulations. (b) and (b') illustrate the cases when the bump generates a repulsive potential resulting in the skyrmion displacement from the central point. The origin of the pinning/repulsive potentials is qualitatively sketched on inset (c): in comparison to the planar case ($\mathcal{A} = 0$), the magnetization inside the dashed oval is more uniform (costs less exchange energy) and less uniform (costs more exchange energy) for the cases $\mathcal{A} > 0$ and $\mathcal{A} < 0$, respectively. Arrows in (a'), (b), (b'), and (c) show the magnetization. Panel (d) shows the bump profile, the geometrical definition of the parameter s , and functions $r(s)$, $z(s)$.

axis of revolution \hat{z} and from the xy -plane, respectively. The curvilinear properties of the surface σ are represented by the principal curvatures $k_1 = z''/r'$, $k_2 = z'/r$. The prime denotes the derivatives with respect to s throughout the entire paper. Note that $k_1(0) = k_2(0) = z''(0)$.

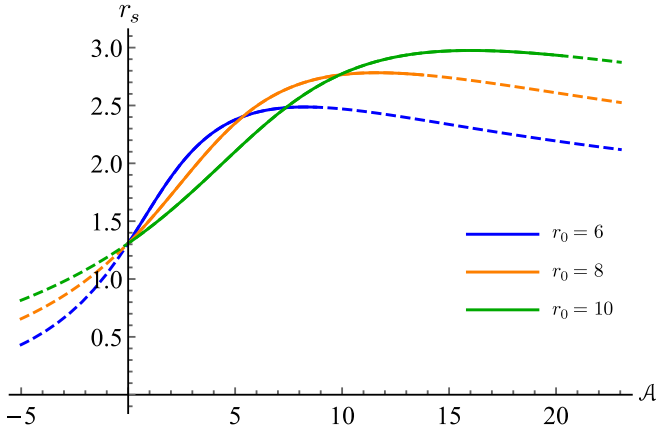


FIG. 2. Skyrmion radius as a function of the bump amplitudes for several different bump widths. The solid and dashed parts of the lines correspond to the stable and unstable regimes, respectively. The skyrmion radius r_s is defined by the equation $\Theta(r_s) = \pi/2$, where the skyrmion profile is obtained by means of numerical solutions of Eq. (3).

III. STATIC SKYRMIONS

Utilizing the constraint $|m| = 1$ by means of the angular parametrization $\mathbf{m} = \sin \theta (\hat{s} \cos \phi + \hat{\chi} \sin \phi) + \hat{n} \cos \theta$ with $\mathbf{n} = [\hat{s} \times \hat{\chi}]$ being the unit normal, one can show that Eq. (2) has the static skyrmion solution in form of $\theta = \Theta(s)$ for $\phi = \Phi = 0$. The skyrmion profile is determined by the following equation [32]:

$$\nabla_s^2 \Theta - \sin \Theta \cos \Theta \Xi + \frac{r'}{r} \sin^2 \Theta (d - 2k_2) = \mathcal{H}', \quad (3)$$

where, $d = D/\sqrt{AK_u}$ is the dimensionless DMI constant, $\mathcal{H} = k_1 + k_2$ is the mean curvature, and $\Xi = 1 + r^{-2} - 2k_2^2 + d\mathcal{H}$. In Eq. (3) and in the following all distances are measured in units of the magnetic length ℓ . The radial part of the Laplace operator reads as $\nabla_s^2 f = r^{-1}(rf)'$. Equation (3) is solved with boundary conditions $\Theta(0) = \pi$, $\Theta(\infty) = 0$. Note that these boundary conditions correspond to the case of a relatively small curvature, when the multiplet of states are not allowed for the skyrmions [32]. Only singlet skyrmion states are therefore considered in this paper.

An example of a skyrmion profile generated by Eq. (3) for the case of a Gaussian bump

$$z = \mathcal{A}e^{-r^2/(2r_0^2)} \quad (4)$$

is shown in Fig. 1(a). As one may note, the skyrmion pinned on the bump has larger radius as compared to the planar case for the same intrinsic DMI and other material parameters. This effect can be interpreted as a result of an enhanced total DMI due to the curvature-induced effective DMI [24,25,30]. For the case $\mathcal{A} < 0$ (concavity), the curvature-induced DMI changes its sign decreasing the total DMI. This in turn decreases the skyrmion radius, see Fig. 1(b) for $\mathcal{A} = -2$ and Fig. 2. With further increasing the negative amplitude of the concavity the intrinsic DMI is fully compensated by the curvature induced DMI and the skyrmion solution collapses to a point singularity. This effect was described previously for skyrmions on spherical shells [30].

For a positive DMI constant, the curvature-induced effective DMI enhances the intrinsic DMI resulting in the skyrmion radius increase, see Fig. 2. For $d < 4/\pi$, a broad range of amplitudes $0 < \mathcal{A} < \mathcal{A}_{\max}(r_0, d)$ exists, for which the stable solution is a skyrmion centered on the bump (see Fig. 3 in Ref. [32], which shows the diagram of skyrmion states on a Gaussian bump). For small negative \mathcal{A} values, the center point of the bump becomes an unstable equilibrium position for the skyrmions. This instability effect originates from the exchange interaction, as qualitatively explained in Fig. 1(c). Namely, the spatial deformation of the film can reduce, as well as enlarge, the spatial gradients of the magnetization.

Skyrmions can be again stabilized on the bump center for large negative \mathcal{A} values. However, in this case several skyrmion solutions (multiplet) may appear, e.g., a doublet with small and large skyrmion radii, as reported previously in Ref. [32]. Alternatively, to stabilize skyrmions on the bump with negative amplitude (concave), one has to consider a negative DMI constant. This changes the skyrmion helicity to $\Phi = \pi$ and reverts the energies of the cases with $\mathcal{A} > 0$ and $\mathcal{A} < 0$ shown in Fig. 1(c).

If a large-radius skyrmion is centered on the bump, the magnetization is not uniform in the skyrmion central area. This is because the magnetization tends to align to the normal direction due to the easy-normal anisotropy. This is in contrast to the planar case. With the increase of the amplitude \mathcal{A} , the magnetization nonuniformity increases resulting in an increase of the exchange energy. Finally, for $\mathcal{A} > \mathcal{A}_{\max}$ the central equilibrium becomes unstable and the skyrmion shifts to the side of the bump, as shown in Fig. 1(b'). This is in line with the previous predictions [32]. So far from the Figs. 1(a'), 1(b), and 1(b') we can conclude that the theoretical predictions and the full-scale finite element micromagnetic simulations are in good agreement. For the technical details of the simulations see Appendix C.

IV. SPECTRUM EVALUATION

In the following let us consider an equilibrium skyrmion state centered on the bump. To study the spectrum of its linear excitations, we introduce small deviations in ϑ and φ : $\theta = \Theta + \vartheta$, $\phi = \Phi + \varphi/\sin \Theta$. For the case of zero damping $\eta = 0$, Eq. (2) can be linearized with respect to the excitations and results in

$$\begin{cases} \partial_\tau \varphi = -\nabla^2 \vartheta + U_1 \vartheta + W \partial_\chi \varphi, \\ -\partial_\tau \vartheta = -\nabla^2 \varphi + U_2 \varphi - W \partial_\chi \vartheta. \end{cases} \quad (5)$$

The dimensionless time is introduced as $\tau = t\Omega_0$, where $\Omega_0 = 2\gamma_0 K_u/M_s$. The Laplace operator has the form $\nabla^2 = \nabla_s^2 + r^{-2}\partial_{\chi\chi}^2$ and potentials have the following expressions [32]:

$$\begin{aligned} U_1 &= \cos 2\Theta \Xi - \frac{r'}{r} \sin 2\Theta (d - 2k_2), \\ U_2 &= \cos^2 \Theta \Xi - \Theta'^2 + k_2^2 - k_1^2 - \Theta'(d - 2k_1) \\ &\quad - \frac{r'}{r} \sin \Theta \cos \Theta (d - 2k_2), \\ W &= 2\frac{r'}{r^2} \cos \Theta - \frac{1}{r} \sin \Theta (d - 2k_2). \end{aligned} \quad (6)$$

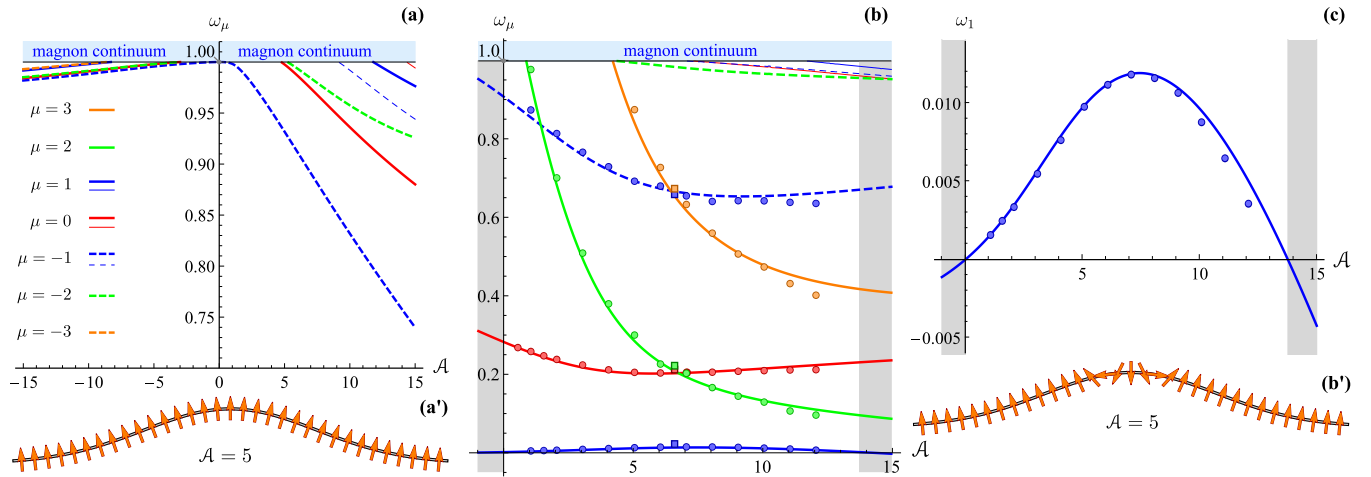


FIG. 3. Eigenfrequencies of the localized eigenstates as functions of the bump amplitude \mathcal{A} are obtained by means of numerical solution of EVP (7) for the Gaussian bump (4) with constant width $r_0 = 8$ and are shown by lines. The markers show the eigenfrequencies obtained by means of micromagnetic simulations. The square-shaped markers correspond to the simulations with the full-scale magnetostatics taken into account. The value of dimensionless DMI constant is $d = 0.98$. The quasinormal and skyrmion equilibrium states obtained from Eq. (3) are shown on panels (a') and (b') for a particular bump height $\mathcal{A} = 5$. The magnon excitation frequencies of the quasinormal and skyrmion states are summarized in (a) and (b) in function of the bump amplitude. Inset (c) is focused to the gyromode ($\mu = 1$). The thin lines are eigenstate solutions whose functions f and g have a node along the radial coordinate s , see Fig. 5. The gray-shadowed rectangles denote the ranges of bump amplitudes ($\mathcal{A} < 0$ and $\mathcal{A} > \mathcal{A}_{\max} \approx 13.77$) for which the bump center is not a stable equilibrium position of the skyrmion.

The solution of Eq. (5) is $\vartheta = f(s) \cos(\omega\tau + \mu\chi + \eta)$, $\varphi = g(s) \sin(\omega\tau + \mu\chi + \eta)$, where $\mu \in \mathbb{Z}$ is the azimuthal wave number and η is an arbitrary phase. The eigenfrequencies ω and the corresponding eigenfunctions f, g are determined by the following generalized eigenvalue problem (EVP):

$$\hat{H}\psi = \omega\hat{\sigma}_1\psi. \quad (7)$$

Here $\psi = (f, g)^T$,

$$\hat{H} = \begin{pmatrix} -\nabla_s^2 + \frac{\mu^2}{r^2} + U_1 & \mu W \\ \mu W & -\nabla_s^2 + \frac{\mu^2}{r^2} + U_2 \end{pmatrix}, \quad (8)$$

and $\hat{\sigma}_1$ is the first Pauli matrix. In the limited case of a planar film ($k_1 = k_2 \equiv 0$ and $r' \equiv 1$) the formulated eigenvalue problem coincides with that formulated previously in Ref. [33] for planar skyrmions.

An example of numerical solution of EVP is shown in Fig. 3. The eigenfunctions and their properties are listed in Appendix A. To find out the influence of the curvature on the magnon spectrum, Gaussian bumps with constant width r_0 and varying bump amplitudes \mathcal{A} have been considered. Only spatially localized eigenstates are investigated. For the ground state, which is the quasinormal magnetization, a number of resonances located closely to the bottom edge of the magnon continuum appears, see Fig. 3(a). The strong asymmetry of the spectra with respect to the change of sign of \mathcal{A} (and the sign of \mathcal{H}) is related to the corresponding change of sign of the effective curvature induced DMI. This effect is also responsible for the strong asymmetry in the skyrmion radius, see Fig. 1 and the discussion above. For more details about the influence of DMI on the magnon spectra see Ref. [43]. In the planar thin-film limit $\mathcal{A} \rightarrow 0$ all localized states with $\mu \neq -1$ disappear. At the specific point of $\mathcal{A} = 0$ the counterclockwise (CCW) mode $\mu = -1$ transforms to the Kittel mode with $\omega_{-1} = 1$ and $f = g = \text{const}$. [44]. A close relation

of the CCW localized mode and Kittel mode was previously indicated in Ref. [45].

The presence of the curvature significantly enriches the spectrum of the localized magnon states, see Fig. 3(b). By means of the comparison to the previously studied skyrmion spectrum for a planar films, the following curvature-induced effects can be distinguished. (i) First of all, it should be noted that due to the breaking of the translation symmetry the translational skyrmion mode ($\mu = 1$) is transformed to the gyromode with small but nonzero frequency ω_1 , see Fig. 3(c). The cases $\omega_1 > 0$ and $\omega_1 < 0$ describe clockwise and counterclockwise skyrmion gyrations, respectively. The latter case corresponds to the repulsive effective potential or in other words—to the unstable equilibrium position at the bump center. (ii) With increasing curvature higher modes with $\mu = \pm 2$ (elliptic modes) and $\mu = 3$ are generated. (iii) In contrast to the planar case the additional quantization of the localized modes in the radial direction is possible, see Fig. 5. In Fig. 3, the corresponding eigenfrequencies are shown by thin lines. (iv) Curvature leads to significant lowering of the CCW mode with $\mu = -1$, making feasible its experimental study [45]. In part, the effect of the frequency lowering can be attributed to the increase of the skyrmion radius, see Fig. 2. Previously it was shown [33,46] that the eigenfrequencies of the localized skyrmion modes goes down with increase of skyrmion radius.

V. COLLECTIVE VARIABLE APPROACH FOR THE GYROMODE

Let us consider the low curvature limit $1 \gg |\mathcal{H}|r_s \gg |\mathcal{K}|r_s^2$, where \mathcal{K} is the Gaussian curvature and r_s is the skyrmion radius defined as $\Theta(r_s) = \pi/2$. In this particular case the motion of the skyrmion can be described using

the rigid particle assumption, modeling the curvature as a perturbative potential that has no influence on the skyrmion profile. In terms of the above-introduced dimensionless units for the length and time, the corresponding Thiele equation (see Appendix B for the derivation) reads as

$$[\mathbf{n} \times \partial_\tau \mathbf{R}] = \frac{\partial \mathcal{E}}{\partial \mathbf{R}} + \bar{\eta} \partial_\tau \mathbf{R}, \quad (9)$$

taking into account that the topological charge of the considered skyrmion on the plane is $N_{\text{top}} = -1$. The topological charge is a crucial quantity for the skyrmion dynamics in terms of collective coordinates because it determines the amplitude of the gyrovector. One can show (see Appendix B) that in the limit case of small curvature, the gyrovector amplitude approaches its planar value, see Eq. (B19). Thus, the planar topological charge can be used in this limit. The generalization of the skyrmion topological charge for an arbitrary curvature is an open question. In Ref. [30], the degree Q of the map $\sigma \mapsto S^2$ realized by the unit field \mathbf{m} on σ was proposed for such a generalization. Although Q is an integer number which is invariant with respect to the continuous deformation of the magnetization, it is important to note that Q is not reflecting the dynamical properties of skyrmions in terms of the collective coordinates. This is reflected by Eq. (B5), see also the discussion after Eq. (B12) in Appendix B.

The total energy of the system $\mathcal{E} = E/E_0$ is measured in units of $E_0 = 8\pi AL$, the position vector $\mathbf{R} = \sigma(X^1, X^2)$ determines the skyrmion center, which has the curvilinear coordinates X^1 and X^2 on the surface. In the considered small curvature limit one can show that (see Appendix B)

$$\mathcal{E} \approx C \mathcal{H}(X^1, X^2) + \mathcal{E}_0, \quad (10)$$

where energy \mathcal{E}_0 is independent on the collective coordinates (X^1, X^2) . The constant C is determined by the equilibrium skyrmion profile $\Theta_{\text{pl}}(s)$ for the case of a planar film, namely $C = C_1 + C_2 d$, where constants C_1 and C_2 have form $C_1 = \frac{1}{4} \int_0^\infty [\Theta_{\text{pl}}(s) - \sin \Theta_{\text{pl}}(s) \cos \Theta_{\text{pl}}(s)] ds$, $C_2 = \frac{1}{4} \int_0^\infty s \sin^2 \Theta_{\text{pl}}(s) ds$. Note that both exchange and DMI interactions make contribution to the first term in Eq. (10). The normalized damping constant $\bar{\eta} = C_0 \eta$ in Eq. (9) is also determined by the planar skyrmion profile: $C_0 = \frac{1}{4} \int_0^\infty [(\partial_s \Theta_{\text{pl}})^2 + s^{-2} \sin^2 \Theta_{\text{pl}}] s ds$. Note that the energy expression (10) is correct for Néel skyrmions only. For the case of a Bloch skyrmion one should take into account the quadratic terms in the curvature, which are neglected in the current study, see Appendix B 3 for details.

To handle Eq. (9), one should note that $\partial_\tau \mathbf{R} = \mathbf{g}_\alpha \partial_\tau X^\alpha$ and $\frac{\partial \mathcal{E}}{\partial \mathbf{R}} = \mathbf{g}^\alpha \frac{\partial \mathcal{E}}{\partial X^\alpha}$, where $\mathbf{g}_\alpha = \partial_\alpha \sigma$, $\alpha \in \{1, 2\}$ is the tangent curvilinear basis and \mathbf{g}^α is the corresponding dual basis.

Applying Eqs. (9) and (10) for the surface of rotation $\sigma = \sigma(s, \chi)$, one can show that the trajectory of motion of the skyrmion center $s = s(\chi)$ is determined by the following relation:

$$\int_{s_0}^{s(\chi)} \frac{ds'}{r(s')} = \bar{\eta}(\chi - \chi_0), \quad (11)$$

where (s_0, χ_0) is the initial skyrmion position. In the vicinity of the central point $s = 0$ the trajectory in Eq. (11) is approximated by a spiral $s(\chi) \approx s_0 e^{\bar{\eta}(\chi - \chi_0)}$. The velocity of the

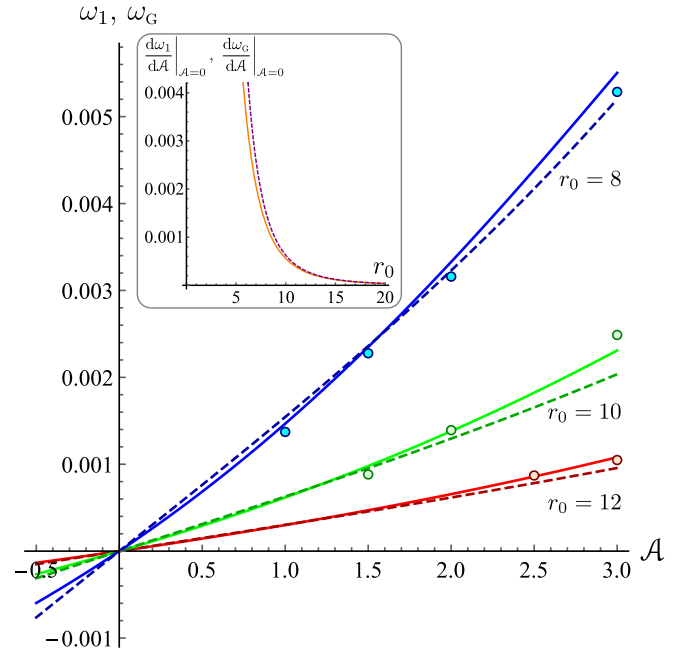


FIG. 4. Frequency of the skyrmion gyromotion in the vicinity of the center of the low-amplitudes bumps in Eq. (4) for three different bump radii are obtained in three different ways: (i) by means of numerical solution of EVP in Eq. (7) for $\mu = 1$ (solid lines), (ii) by means of the collective variable approximation (13) (dashed lines), and (iii) by means of micromagnetic simulations (markers). For all cases $d = 0.98$ which results in $C \approx 1.556$. The inset demonstrates the slope in the point $A = 0$, the dashed line corresponds to the approximation $d\omega_G/dA|_{A=0} \approx 4C/r_0^4$.

skyrmion therefore is

$$\mathbf{v} = -\frac{C\mathcal{H}'(s)}{1 + \bar{\eta}^2} \left[\bar{\eta} \frac{r'(s)}{r(s)} \hat{\mathbf{s}} + \hat{\boldsymbol{\chi}} \right]. \quad (12)$$

As it follows from Eq. (12), the skyrmion is immobile on a surface with constant mean curvature (e.g., surface of a sphere, minimal surface). The central point $s = 0$ is a stationary point which is stable (unstable) if $\mathcal{H}''(0) > 0$ [$\mathcal{H}''(0) < 0$]. This result supports the qualitative explanations of the skyrmion stability shown in Fig. 1(c).

For zero damping the skyrmion rotates around the stationary point with constant frequency $\omega_G = C\mathcal{H}'(s_0)/r(s_0)$, which is determined by the initial skyrmion displacement. Here the positive frequency sign corresponds to the clockwise rotation. In the limiting case of infinitesimal displacements $s_0 \rightarrow 0$, the skyrmion gyration is described by the magnon mode with $\mu = 1$, which was discussed in the previous section. In this case

$$\omega_1 = \omega_G \approx C\mathcal{H}''(0). \quad (13)$$

For the Gaussian bump (4) one has $\mathcal{H}''(0) = 4\frac{A}{r_0^4}(1 + \frac{A^2}{r_0^2})$. The corresponding comparison of the collective variable approach predictions in Eq. (13) for ω_G , the numerical calculations for ω_1 , and the gyromode frequencies from micromagnetic simulations for three different frequencies are shown in Fig. 4. Please note the good agreement between the collective coordinates and the EVP solutions. The small

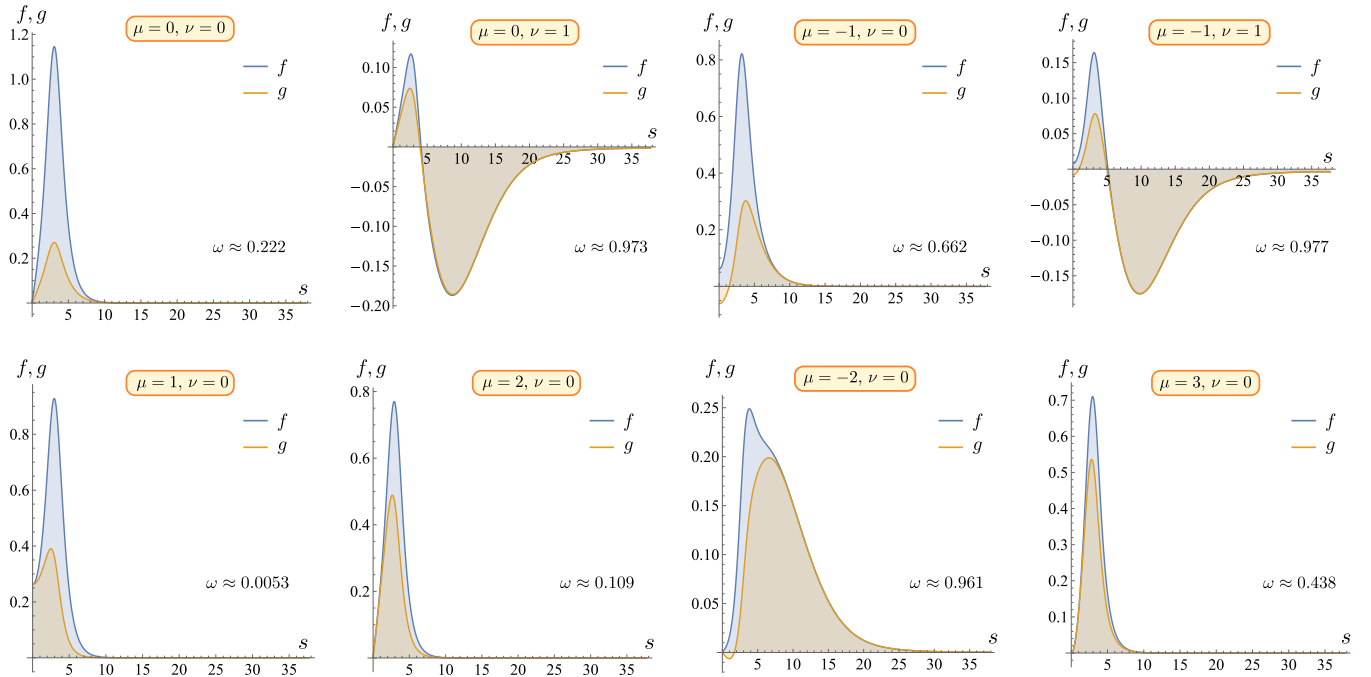


FIG. 5. Eigenfunctions of the localized modes shown in Fig. 3(b) for the bump amplitude $\mathcal{A} = 12$. μ and ν denote the azimuthal and radial quantum numbers, respectively.

deviation of the slopes $d\omega_G/d\mathcal{A}|_{\mathcal{A}=0}$ and $d\omega_1/d\mathcal{A}|_{\mathcal{A}=0}$, which appear for small r_0 can be explained by the fact that the energy approximation (10), as well as the magnitude of the gyrovector (B19) used in Eq. (9), were obtained under the assumption that the metric is constant within the skyrmion area. This approximation is violated if the skyrmion radius r_s is comparable to the bump width r_0 .

VI. CONCLUSION

We presented an analysis on the influence of the curvature on the spectrum of localized magnon eigenmodes of ferromagnetic skyrmions. We demonstrated that the curvature induces modes with higher azimuthal quantum numbers, which are absent for skyrmions in planar films. Additionally, modes with radial quantum numbers can appear for the skyrmions pinned on a bump.

Interestingly, the translational mode of the skyrmion is transformed into the gyromode by the curvature and has nonzero frequency proportional to the second derivative of the mean curvature at the bump center $\omega_G \propto \mathcal{H}''(0)$. For small amplitude Gaussian bumps (4) the following simple relation is found: $\omega_G \propto \mathcal{A}/r_0^4$. We showed that these analytical estimations can be obtained with the Thiele equation, which we generalized for the case of skyrmions on an arbitrary curvilinear shell. Furthermore, we demonstrated that Néel skyrmions experience the curvature-induced driving force proportional to the gradient of the mean curvature.

ACKNOWLEDGMENTS

We thank Denys Makarov for the fruitful discussions. A. Kornienko acknowledges financial support from DAAD (Leonhard Euler Program, Project No. 57430566). A. Kákay

acknowledges the financial support of within the DFG program KA 5069/1-1. D. Sheka acknowledges the financial support from the Alexander von Humboldt Foundation (Research Group Linkage Program) and the DFG program MA 5144/22-1. In part, this work was supported by the Program of Fundamental Research of the Department of Physics and Astronomy of the National Academy of Sciences of Ukraine (Project No. 0120U100855), by Taras Shevchenko National University of Kyiv (Project No. 19BF052-01).

APPENDIX A: EIGENFUNCTIONS

Some examples of eigenfunctions $f(s)$ and $g(s)$ of localized eigenmodes are shown in Fig. 5. In contrast to the localized modes of the planar skyrmion, the additional quantization in radial direction ($\nu > 0$) takes place for the skyrmion on a bump.

Eigenfunctions f and g satisfy orthogonality condition (for given μ)

$$\int_0^\infty [f_{\mu,\nu}(s)g_{\mu,\nu'}(s) + f_{\mu,\nu'}(s)g_{\mu,\nu}(s)]r(s)ds = \delta_{\nu,\nu'}, \quad (\text{A1})$$

which is similar as for the case of a planar skyrmion [33].

APPENDIX B: CURVILINEAR GENERALIZATION OF THIELE EQUATION

1. General three-dimensional case

Assume that magnetization $\mathbf{m}(\mathbf{r}, t)$ in some three-dimensional (3D) space domain $\boldsymbol{\tau}$ can be presented in form $\mathbf{m} = \mathbf{m}(\mathbf{r}, X^1(t), X^2(t), \dots)$ where $X^i(t)$ are some collective variables. Multiplying the Landau-Lifshitz equation (2) first by $\partial\mathbf{m}/\partial X^i \times (\dots)$ then by $\mathbf{m} \cdot (\dots)$ and then integrating

over the space domain τ one obtains the well-known [47,48] collective variable equation

$$\mathbb{G}_{ij}\partial_t X^j = \frac{\partial E}{\partial X^i} + \eta \mathbb{D}_{ij}\partial_t X^j, \quad (\text{B1})$$

where

$$\mathbb{G}_{ij} = \frac{M_s}{\gamma_0} \int_{\tau} \mathbf{m} \cdot \left(\frac{\partial \mathbf{m}}{\partial X^i} \times \frac{\partial \mathbf{m}}{\partial X^j} \right) dV, \quad (\text{B2a})$$

$$\mathbb{D}_{ij} = \frac{M_s}{\gamma_0} \int_{\tau} \frac{\partial \mathbf{m}}{\partial X^i} \cdot \frac{\partial \mathbf{m}}{\partial X^j} dV, \quad (\text{B2b})$$

with dV being the volume element. Let us assume now that there exists a curvilinear frame of reference $\{\xi^1, \xi^2, \xi^3\}$ in τ such that the magnetization dynamics can be presented in the form of a traveling wave

$$\mathbf{m}^i = m^i(\xi^1 - X^1, \xi^2 - X^2, \xi^3 - X^3). \quad (\text{B3})$$

Here $\mathbf{m} = m^i \tilde{\mathbf{g}}_i$, where $\tilde{\mathbf{g}}_i = \partial_i \tau$ is covariant (tangent) basis [49] induced by the parametrization $\tau = \tau(\xi^1, \xi^2, \xi^3)$. The shortening $\partial_i = \partial_{\xi^i}$ is used here and below. Note that the traveling-wave model formulated for the Cartesian coordinates and for Cartesian magnetization components describes only translations in 3D space and do not describe possible soliton rotations. These last can be taken into account by introducing a curvilinear frame of reference whose local basis rotates together with the soliton.

Since the equation (B1) is derived in coordinate-independent way, it keeps its form for any frame of reference. The tensors (B2) now read

$$\mathbb{G}_{ij} = \frac{M_s}{\gamma_0} \int_{\tau} \varepsilon_{klm} m^k \partial_i m^l \partial_j m^m dV, \quad (\text{B4a})$$

$$\mathbb{D}_{ij} = \frac{M_s}{\gamma_0} \int_{\tau} \tilde{g}_{kl} \partial_i m^k \partial_j m^l dV. \quad (\text{B4b})$$

Here $\tilde{g}_{kl} = \tilde{\mathbf{g}}_k \cdot \tilde{\mathbf{g}}_l$ is the metric tensor and $\varepsilon_{klm} = \sqrt{|\tilde{g}|} \varepsilon_{klm}$ is the Levi-Civita tensor, with $\tilde{g} = \det ||\tilde{g}_{ij}||$ and ε_{klm} being the Levi-Civita symbol. We also took into account that $\partial_X m^k = -\partial_i m^k$. It is important to note that derivatives in Eq. (B4) are not covariant and for this reason generally

$$\varepsilon_{klm} m^k \partial_i m^l \partial_j m^m \neq \mathbf{m} \cdot [\partial_i \mathbf{m} \times \partial_j \mathbf{m}]. \quad (\text{B5})$$

The equality in Eq. (B5) takes place only for Euclidian metric when \tilde{g}_{kl} are coordinate independent, e.g., for Cartesian frame of reference.

Since tensor \mathbb{G}_{ij} is by definition antisymmetric, one can write $\mathbb{G}_{ij} = \varepsilon_{ijk} G^k$. By means of the gyrovector $\mathbf{G} = \tilde{\mathbf{g}}_k G^k$ one can rewrite Eq. (B1) in a common Thiele form

$$[\partial_t \mathbf{R} \times \mathbf{G}] = \frac{\partial E}{\partial \mathbf{R}} + \eta \mathbf{D} \partial_t \mathbf{R}. \quad (\text{B6})$$

Here we introduced the notation $\tilde{\mathbf{g}}_i \partial_i X^i = \partial_t \mathbf{R}$, which defines \mathbf{R} as a vector of the soliton position

$$\mathbf{R} = \tau(X^1, X^2, X^3). \quad (\text{B7})$$

We also introduced the notation

$$\frac{\partial E}{\partial \mathbf{R}} = \tilde{\mathbf{g}}^j \frac{\partial E}{\partial X^j}, \quad (\text{B8})$$

which is consistent with Eq. (B7), here $\tilde{\mathbf{g}}^i$ are vectors of the dual basis. Indeed, using Eq. (B7) one can write $\partial E / \partial X^i = (\partial E / \partial \mathbf{R}) \cdot (\partial \mathbf{R} / \partial X^i) = (\partial E / \partial \mathbf{R}) \cdot \tilde{\mathbf{g}}_i$. Multiplying this equation by $\tilde{\mathbf{g}}^i$ and using the identity $\mathbf{a} = \tilde{\mathbf{g}}^i (\mathbf{a} \cdot \tilde{\mathbf{g}}_i)$ one obtains Eq. (B8). The damping tensor is $\mathbf{D} = \mathbb{D}_{ij} \tilde{\mathbf{g}}^i \otimes \tilde{\mathbf{g}}^j$ [50]. Components of the gyrovector can be expressed as follows [51]

$$G^i = \frac{1}{2} \varepsilon^{ijk} \mathbb{G}_{jk}. \quad (\text{B9})$$

Note that all quantities in this equation generally depend on X^1, X^2, X^3 .

2. Thin curvilinear shell

Let us consider the space domain in form of curvilinear shell of thickness L

$$\tau(\xi^1, \xi^2, \xi^3) = \sigma(\xi^1, \xi^2) + \mathbf{n}(\xi^1, \xi^2) \xi^3, \quad (\text{B10})$$

where $\sigma(\xi^1, \xi^2)$ is the central shell surface, $\xi^3 \in [-L/2, L/2]$, and $\mathbf{n} = \mathbf{g}_1 \times \mathbf{g}_2 / \sqrt{|g|}$ is the unit normal to the surface. Here $\mathbf{g}_\alpha = \partial_\alpha \sigma = \lim_{\xi^3 \rightarrow 0} \tilde{\mathbf{g}}_\alpha$ is the covariant (tangent) basis on the surface. Here and below Greek indices take values $\{1, 2\}$, while Latin indices take the values $\{1, 2, 3\}$. $g = \det ||g_{\alpha\beta}||$, with $g_{\alpha\beta} = \mathbf{g}_\alpha \cdot \mathbf{g}_\beta$ being the surface metric tensor.

Let magnetization in τ satisfies the condition (B3) and does not depend on ξ^3 . Consequently, the total energy E does not depend on X^3 . In this case one can easily show that the Thiele equation (B6) is fulfilled if $X^3 \equiv 0$ [52], i.e.,

$$\mathbf{R} = \sigma(X^1, X^2). \quad (\text{B11})$$

Since magnetization does not depend on ξ^3 , according to Eqs. (B9) and (B4a) one has $\mathbf{G} = G^3 \tilde{\mathbf{g}}_3 = G \mathbf{n}$, where $G = G^3$ is the amplitude of the gyrovector

$$G = \frac{M_s}{\gamma_0} \frac{L}{\sqrt{|g(X^1, X^2)|}} \int_{\sigma} \sqrt{|g(\xi^1, \xi^2)|} \begin{vmatrix} m^1 & m^2 & m^3 \\ \partial_1 m^1 & \partial_1 m^2 & \partial_1 m^3 \\ \partial_2 m^1 & \partial_2 m^2 & \partial_2 m^3 \end{vmatrix} dS + (\text{higher terms in } L), \quad (\text{B12})$$

where $dS = \sqrt{|g|} d\xi^1 d\xi^2$ is the element of the surface area. For a constant magnetization (in the curvilinear frame of reference), the integrand in Eq. (B12) vanishes as well as the left-hand side of Eq. (B5). However, the right-hand side of Eq. (B5) generally does not vanish, e.g., it is the Gaussian curvature for the normal magnetization ($m^1 = m^2 = 0, m^3 = 1$). The linear in L part of the dissipative tensor is $\mathbf{D} = D_{\alpha\beta} \mathbf{g}^\alpha \otimes \mathbf{g}^\beta$, where

$$D_{\alpha\beta} = \frac{M_s}{\gamma_0} L \int_{\sigma} (g_{\mu\nu} \partial_\alpha m^\mu \partial_\beta m^\nu + \partial_\alpha m^3 \partial_\beta m^3) dS. \quad (\text{B13})$$

Here we also utilized the independence of magnetization on ξ^3 .

If the basis vectors \mathbf{g}_1 and \mathbf{g}_2 are orthogonal then one can introduce the angular parametrization for the

magnetization: $\sqrt{g_{11}}m^1 = \sin\theta \cos\phi$, $\sqrt{g_{22}}m^2 = \sin\theta \sin\phi$, and $m^3 = \cos\theta$. In this case one obtains

$$G = \frac{M_s}{\gamma_0} \frac{L}{\sqrt{|g(X^1, X^2)|}} \int_{\sigma} \sqrt{|g(\xi^1, \xi^2)|} \mathcal{G} \cdot d\mathbf{S}, \quad (\text{B14a})$$

$$\mathcal{G} = \sin\theta[\nabla\theta \times \nabla\phi] + \sin\theta \sin\phi \cos\phi \left[\nabla\theta \times \nabla \ln \sqrt{\frac{g_{11}}{g_{22}}} \right] + \sin^2\theta \cos\theta [\nabla\phi \times (\cos^2\phi \nabla \ln \sqrt{g_{11}} + \sin^2\phi \nabla \ln \sqrt{g_{22}})] + \sin^2\theta \cos\theta \sin\phi \cos\phi \times [\nabla \ln \sqrt{g_{11}} \times \nabla \ln \sqrt{g_{22}}], \quad (\text{B14b})$$

where $\nabla = \mathbf{g}^\alpha \partial_\alpha$ is the surface del operator and $d\mathbf{S} = n dS$. For the case of the Euclidean (coordinate independent) metric the expression (B14) transforms into the familiar [53,54] formula

$$G^E = \frac{M_s}{\gamma_0} L \int_{\sigma} \sin\theta [\nabla\theta \times \nabla\phi] \cdot d\mathbf{S}. \quad (\text{B15})$$

However, in general the case of the non-Euclidean metric the amplitude of the gyrovector can deviate from the value of Eq. (B15).

For angular parametrization the elements of the dissipative tensor (B13) are as follows:

$$D_{\alpha\beta} = \frac{M_s L}{\gamma_0} \frac{1}{2} \int_{\sigma} \left[\partial_\alpha \theta \partial_\beta \theta + \sin^2\theta (\partial_\alpha \phi \partial_\beta \phi + \cos^2\phi \partial_\alpha \ln \sqrt{g_{11}} \partial_\beta \ln \sqrt{g_{11}} + \sin^2\phi \partial_\alpha \ln \sqrt{g_{22}} \partial_\beta \ln \sqrt{g_{22}}) - \sin 2\theta \partial_\alpha \theta (\cos^2\phi \partial_\beta \ln \sqrt{g_{11}} + \sin^2\phi \partial_\beta \ln \sqrt{g_{22}}) - \sin^2\theta \sin 2\phi \partial_\alpha \phi \partial_\beta \ln \sqrt{\frac{g_{22}}{g_{11}}} + (\alpha \leftrightarrow \beta) \right] dS. \quad (\text{B16})$$

For a Euclidean metric Eq. (B16) is reduced to the familiar formula

$$D_{\alpha\beta}^E = \frac{M_s}{\gamma_0} L \int_{\sigma} (\partial_\alpha \theta \partial_\beta \theta + \sin^2\theta \partial_\alpha \phi \partial_\beta \phi) dS. \quad (\text{B17})$$

3. Skyrmion in thin curvilinear shell

Let us assume that we were able to introduce an orthogonal frame of reference $\{\xi^1, \xi^2\}$ on the surface, such that the skyrmion motion can be described by means of the following Ansatz:

$$\theta = \Theta_{\text{pl}} \left(\sqrt{g_{11}(\xi^1 - X^1)^2 + g_{22}(\xi^2 - X^2)^2} \right), \quad (\text{B18a})$$

$$\phi = \arctan \frac{\sqrt{g_{22}}(\xi^2 - X^2)}{\sqrt{g_{11}}(\xi^1 - X^1)} + \phi_0, \quad (\text{B18b})$$

where $\Theta_{\text{pl}}(r)$ is the skyrmion profile on a plane. The use of the Ansatz (B18) means that we consider curvature as a small perturbation, which does not change the skyrmion profile.

To obtain the value of the gyrovector G , one should substitute Eq. (B18) into Eq. (B14). If the size of the area of localization of the function $\Theta_{\text{pl}}(r)$ —the skyrmion radius r_s —is

comparable to the typical lengthscale of change of the metric, then one should expect the deviation of G from its planar value. However, if the skyrmion radius is small, $r_s \ll 1/|\mathcal{H}|$ and $r_s \ll |\mathcal{H}|/|\mathcal{K}|$, then one can assume that $g_{\alpha\alpha}(\xi^1, \xi^2) \approx g_{\alpha\alpha}(X^1, X^2)$ and $\partial_\beta g_{\alpha\alpha}(\xi^1, \xi^2) \approx \partial_\beta g_{\alpha\alpha}(X^1, X^2)$ within the skyrmion core. In this case one can make a change of variables $\sqrt{g_{11}}(\xi^1 - X^1) = r \cos\chi$, $\sqrt{g_{22}}(\xi^2 - X^2) = r \sin\chi$ in the integral $\int_{\sigma} dS$ and utilize the spatial localization of the function $\sin\Theta_{\text{pl}}$. Now, after the integration over χ in Eq. (B14a) all terms in Eq. (B14b) but the first one are integrated out. Finally, Eq. (B12) is reduced to Eq. (B15) and one obtains the same result as for the planar case, namely,

$$G = \frac{M_s}{\gamma_0} L 4\pi N_{\text{top}}, \quad (\text{B19})$$

with N_{top} being topological charge of the *planar* skyrmion.

Using the same technique one obtains for the dissipative tensor

$$D_{\alpha\beta} = \frac{M_s}{\gamma_0} L 4\pi [C_0 g_{\alpha\beta} + C_2 (\Gamma_{\alpha 1}^1 \Gamma_{\beta 1}^1 + \Gamma_{\alpha 2}^2 \Gamma_{\beta 2}^2)], \quad (\text{B20})$$

where $C_0 = \frac{1}{4} \int_0^\infty [(\partial_r \Theta_{\text{pl}})^2 + r^{-2} \sin^2 \Theta_{\text{pl}}] r dr$, $C_2 = \frac{1}{4} \int_0^\infty \sin^2 \Theta_{\text{pl}} r dr$, and $\Gamma_{\alpha\beta}^\gamma$ denote the Christoffel symbol of the second kind. Thus, for the surface with the non-Euclidean metric the dissipative tensor is generally nondiagonal even for a small-radius skyrmion. Note that in the limiting case $r_s \rightarrow 0$ one has $C_0 \rightarrow 1$ and $C_2 \rightarrow 0$.

For the dimensionless time and coordinates introduced in the main text, one writes Thiele Eq. (B6) in form (9) if the gyrovector amplitude (B19) is used for $N_{\text{top}} = -1$, and the term with C_2 is neglected in the damping tensor (B20). This last corresponds to the assumption $C_2 \ll C_0$.

Let us estimate the curvature-induced corrections to the energy of the skyrmion. To estimate the exchange energy $E_x = AL \int \mathcal{E}_x dS$ we use the previously derived [24] expression for the exchange energy density

$$\mathcal{E}_x = [\nabla\theta - \mathbf{\Gamma}]^2 + [\sin\theta(\nabla\phi - \mathbf{\Omega}) - \cos\theta \partial_\phi \mathbf{\Gamma}]^2. \quad (\text{B21})$$

Here $\mathbf{\Gamma} = \mathbf{g}^\alpha b_{\alpha\beta} m_{\parallel}^\beta(\phi)$. Where $b_{\alpha\beta}$ is the second fundamental form and $m_{\parallel}^\beta = m^\beta(\theta = \pi/2)$ are the magnetization components for the strictly tangential magnetization, namely, $m_{\parallel}^1(\phi) = \cos\phi/\sqrt{g_{11}}$ and $m_{\parallel}^2(\phi) = \sin\phi/\sqrt{g_{22}}$, and $\mathbf{\Omega}$ is the vector of spin connection [24,55]. Using the Ansatz (B18) and applying the same method as for derivation of the gyrovector, one obtains

$$E_x = E_x^0 + 8\pi ALC_1 H \cos\phi_0 + \mathcal{O}(H^2, K, |\mathbf{\Omega}|^2). \quad (\text{B22})$$

Here E_x^0 is the exchange energy of the planar skyrmion, H and K are the mean and Gaussian curvatures, respectively, and $C_1 = \frac{1}{4} \int_0^\infty [\Theta_{\text{pl}} - \sin\Theta_{\text{pl}} \cos\Theta_{\text{pl}}] dr$. Note that the curvature-induced corrections are essentially different for Néel and Bloch skyrmions: for a Bloch skyrmion ($\phi_0 = \pm\pi/2$) the energy (B22) does not have the contribution linear in curvature. To evaluate the quadratic corrections, one should introduce the Riemann normal coordinates [56,57] centered on the skyrmion. In this case, the spin connections are determined only by the Gaussian curvature of the surface and not by the curvature of the curvilinear frame of reference itself. Since

we are interested in the dynamics of the Néel skyrmion, we limit ourselves only with the main term in Eq. (B22) with $\cos \phi_0 = 1$.

Let us now consider the DMI energy $E_D = \mathcal{D}L \int \mathcal{E}_D dS$ with density [30,32]

$$\mathcal{E}_D = 2\partial_\alpha \theta m_{||}^\alpha(\phi) \sin^2 \theta - H \cos^2 \theta. \quad (\text{B23})$$

Applying the same procedure as for the exchange energy one obtains

$$E_D = E_D^0 + 8\pi \mathcal{D}L C_2 H + \text{const.}, \quad (\text{B24})$$

where constant C_2 is determined above.

Within the used approximation the anisotropy energy of the skyrmion is a constant independent of the skyrmion position. Collecting now Eqs. (B22) and (B24), and passing to the dimensionless coordinates and curvature $\mathcal{H} = \ell H$, one obtains expression (10) for the normalized energy.

APPENDIX C: FINITE ELEMENT MICROMAGNETIC SIMULATIONS

To support the theoretical predictions and numerical calculations presented in the paper we performed full-scale finite element micromagnetic simulations. The static equilibrium states of the skyrmions on the Gaussian bumps as well as their excitations were obtained by the numerical integration of the Landau-Lifshitz-Gilbert equation using our finite element micromagnetic simulator TETRAMAG [34]. The following material parameters were considered to mimic a Pt/Co/AlOx layer structure: $A = 1.6 \times 10^{-11}$ J/m being the exchange constant, $\mu_0 M_s = 1.38$ T the saturation magnetization, and $K_u = 1.3 \times 10^6$ J/m³ for the uniaxial anisotropy constant pointing along the surface normal. The effective anisotropy constant for the renormalized magnetostatic case was set to $K^{\text{eff}} = K_u - 2\pi M_s^2 = 5.1 \times 10^5$ J/m³. The magnetic length is therefore $\ell = \sqrt{A/K^{\text{eff}}} = 5.6$ nm.

To study the skyrmion excitations a Gaussian bump defined by Eq. (4) with a thickness of 1 and 200 nm in diameter was used. The bump amplitude and radius varies in the simulations. The static skyrmion profiles were calculated with a Gilbert damping $\alpha = 0.5$, while the skyrmion dynamics is simulated with $\alpha = 0.02$. The energy contribution from the intrinsic DMI is implemented into our micromagnetic simulator TETRAMAG in the following form: $\mathcal{E}_{\text{DMI}} = m_n \nabla \cdot \mathbf{m} - \mathbf{m} \cdot \nabla m_n$ with the corresponding effective field

$\mathbf{H}_{\text{DMI}} = -\frac{2\mathcal{D}}{M_s} [\mathbf{n} \nabla \cdot \mathbf{m} - \nabla(\mathbf{m} \cdot \mathbf{n})]$, where \mathbf{n} is the surface normal vector, $\mathbf{m} = M/M_s$ the unit magnetization vector, m_n the surface normal component of the magnetization vector field, and $\mathcal{D} = 2.8 \times 10^{-3}$ J/m² ($d = 0.98$) being the DMI constant.

Simulations with the full-scale magnetostatics were made for the anisotropy and DMI constants $K_u = 1.6$ MJ/m³ and $\mathcal{D} = 9.4$ mJ/m². The other material parameters are the same as described above. This corresponds to the magnetic length $\ell = 1.67$ nm and the quality factor $Q = K_u/(2\pi M_s^2) = 8.6$. The simulated shell thickness was $h = 0.5$ nm. Keeping the geometrical parameters \mathcal{A} and r_0 unchanged (in dimensionless units) we significantly increase the total size of the simulated sample.

The following fields have been used to excite the different magnon modes of the skyrmion localized to the center of the Gaussian bump.

(1) The skyrmion *gyromotion* (corresponding to the mode with the azimuthal quantum number $\mu = 1$) is excited by applying an inhomogeneous external magnetic field $\mathbf{B} = \hat{z}B_0 x \mathcal{H}(L - \sqrt{x^2 + y^2})/L$, $L = 50$ nm and $B_0 = 50$ mT; the $\mathcal{H}(\bullet)$ is the Heaviside step function.

(2) The *breathing mode* ($\mu = 0$) is excited with a uniform magnetic field, $\mathbf{B} = \hat{z}B_0$ applied for a time duration of about 150 ps and field strength of $B_0 = 50$ mT.

(3) The *CCW gyrotropic mode* ($\mu = -1$) was excited with a uniform field $\mathbf{B} = \hat{x}B_0$ applied for 200 ps and field strength of $B_0 = 50$ mT.

(4) The *elliptical mode* ($\mu = 2$) was excited by an inhomogeneous external magnetic field pulse $\mathbf{B} = \hat{z}B_0 \cos(2\chi) \mathcal{H}(L - \sqrt{x^2 + y^2})$ applied for a time duration of 200 ps and field strength of $B_0 = 50$ mT.

(5) To achieve the excitation of modes with *azimuthal mode* number $\mu = 3$ we applied the following field pulse $\mathbf{B} = \hat{z}B_0 \cos(3\chi) \mathcal{H}(L - \sqrt{x^2 + y^2}) \sqrt{x^2 + y^2}/L$ for a time period of 50 to 100 ps, depending on the bump amplitude and the fields strength was set to $B_0 = 50$ mT.

To determine the mode frequencies we performed a fast Fourier transform of the magnetization of every single discretization node over a relatively long time interval (minimum ten periods of simulations). The power spectra obtained from the eigenvalue problem [Eq. (7)] and with the collective variables approach in Eq. (13) are in perfect agreement with that calculated with the full-scale finite element micromagnetic simulations.

- [1] A. N. Bogdanov and D. A. Yablonskiĭ, Thermodynamically stable “vortices” in magnetically ordered crystals. The mixed state of magnets, Zh. Eksp. Teor. Fiz. **95**, 178 (1989).
- [2] A. Bogdanov and A. Hubert, Thermodynamically stable magnetic vortex states in magnetic crystals, J. Magn. Magn. Mater. **138**, 255 (1994).
- [3] J. P. Liu, Z. Zhang, and G. Zhao, *Skyrmions: Topological Structures, Properties, and Applications (Series in Materials Science and Engineering)* (CRC Press/Taylor & Francis Group, Boca Raton, FL, 2016).

- [4] A. Fert, N. Reyren, and V. Cros, Magnetic skyrmions: Advances in physics and potential applications, Nat. Rev. Mater. **2**, 17031 (2017).
- [5] R. Wiesendanger, Nanoscale magnetic skyrmions in metallic films and multilayers: A new twist for spintronics, Nat. Rev. Mater. **1**, 16044 (2016).
- [6] N. Manton and P. Sutcliffe, *Topological Solitons*, Cambridge Monographs on Mathematical Physics (Cambridge University Press, Cambridge, England, 2004).
- [7] A. Fert, V. Cros, and J. Sampaio, Skyrmions on the track, Nat. Nanotechnol. **8**, 152 (2013).

- [8] J. Sampaio, V. Cros, S. Rohart, A. Thiaville, and A. Fert, Nucleation, stability and current-induced motion of isolated magnetic skyrmions in nanostructures, *Nat. Nanotechnol.* **8**, 839 (2013).
- [9] R. Tomasello, E. Martinez, R. Zivieri, L. Torres, M. Carpentieri, and G. Finocchio, A strategy for the design of skyrmion racetrack memories, *Sci. Rep.* **4**, 6784 (2014).
- [10] X. Zhang, G. P. Zhao, H. Fangohr, J. P. Liu, W. X. Xia, J. Xia, and F. J. Morvan, Skyrmion-skyrmion and skyrmion-edge repulsions in skyrmion-based racetrack memory, *Sci. Rep.* **5**, 7643 (2015).
- [11] S. Krause and R. Wiesendanger, Spintronics: Skyrmionics gets hot, *Nat. Mater.* **15**, 493 (2016).
- [12] W. Kang, Y. Huang, C. Zheng, W. Lv, N. Lei, Y. Zhang, X. Zhang, Y. Zhou, and W. Zhao, Voltage controlled magnetic skyrmion motion for racetrack memory, *Sci. Rep.* **6**, 23164 (2016).
- [13] J. Müller, Magnetic skyrmions on a two-lane racetrack, *New J. Phys.* **19**, 025002 (2017).
- [14] X. Zhang, M. Ezawa, and Y. Zhou, Magnetic skyrmion logic gates: conversion, duplication and merging of skyrmions, *Sci. Rep.* **5**, 9400 (2015).
- [15] S. Mühlbauer, B. Binz, F. Jonietz, C. Pfleiderer, A. Rosch, A. Neubauer, R. Georgii, and P. Böni, Skyrmion lattice in a chiral magnet, *Science* **323**, 915 (2009).
- [16] X. Z. Yu, Y. Onose, N. Kanazawa, J. H. Park, J. H. Han, Y. Matsui, N. Nagaosa, and Y. Tokura, Real-space observation of a two-dimensional skyrmion crystal, *Nature* **465**, 901 (2010).
- [17] X. Z. Yu, N. Kanazawa, Y. Onose, K. Kimoto, W. Z. Zhang, S. Ishiwata, Y. Matsui, and Y. Tokura, Near room-temperature formation of a skyrmion crystal in thin-films of the helimagnet fege, *Nat. Mater.* **10**, 106 (2011).
- [18] P. Milde, D. Kohler, J. Seidel, L. M. Eng, A. Bauer, A. Chacon, J. Kindervater, S. Mühlbauer, C. Pfleiderer, S. Buhrandt, C. Schütte, and A. Rosch, Unwinding of a skyrmion lattice by magnetic monopoles, *Science* **340**, 1076 (2013).
- [19] U. K. Röbber, A. N. Bogdanov, and C. Pfleiderer, Spontaneous skyrmion ground states in magnetic metals, *Nature* **442**, 797 (2006).
- [20] M. Lee, W. Kang, Y. Onose, Y. Tokura, and N. P. Ong, Unusual Hall Effect Anomaly in MnSi under Pressure, *Phys. Rev. Lett.* **102**, 186601 (2009).
- [21] A. Neubauer, C. Pfleiderer, B. Binz, A. Rosch, R. Ritz, P. G. Niklowitz, and P. Böni, Topological Hall Effect in the a Phase of MnSi, *Phys. Rev. Lett.* **102**, 186602 (2009).
- [22] N. Kanazawa, Y. Onose, T. Arima, D. Okuyama, K. Ohoyama, S. Wakimoto, K. Kakurai, S. Ishiwata, and Y. Tokura, Large Topological Hall Effect in a Short-Period Helimagnet MnGe, *Phys. Rev. Lett.* **106**, 156603 (2011).
- [23] Y. Li, N. Kanazawa, X. Z. Yu, A. Tsukazaki, M. Kawasaki, M. Ichikawa, X. F. Jin, F. Kagawa, and Y. Tokura, Robust Formation of Skyrmions and Topological Hall Effect Anomaly in Epitaxial thin Films of MnSi, *Phys. Rev. Lett.* **110**, 117202 (2013).
- [24] Y. Gaididei, V. P. Kravchuk, and D. D. Sheka, Curvature Effects in Thin Magnetic Shells, *Phys. Rev. Lett.* **112**, 257203 (2014).
- [25] D. D. Sheka, V. P. Kravchuk, and Y. Gaididei, Curvature effects in statics and dynamics of low dimensional magnets, *J. Phys. A: Math. Theor.* **48**, 125202 (2015).
- [26] R. Streubel, P. Fischer, F. Kronast, V. P. Kravchuk, D. D. Sheka, Y. Gaididei, O. G. Schmidt, and D. Makarov, Magnetism in curved geometries (topical review), *J. Phys. D* **49**, 363001 (2016).
- [27] A. Crépieux and C. Lacroix, Dzyaloshinsky–Moriya interactions induced by symmetry breaking at a surface, *J. Magn. Magn. Mater.* **182**, 341 (1998).
- [28] A. N. Bogdanov and U. K. Röbber, Chiral Symmetry Breaking in Magnetic Thin Films and Multilayers, *Phys. Rev. Lett.* **87**, 037203 (2001).
- [29] A. Thiaville, S. Rohart, É. Jué, V. Cros, and A. Fert, Dynamics of Dzyaloshinskii domain walls in ultrathin magnetic films, *Europhys. Lett.* **100**, 57002 (2012).
- [30] V. P. Kravchuk, U. K. Röbber, O. M. Volkov, D. D. Sheka, J. van den Brink, D. Makarov, H. Fuchs, H. Fangohr, and Y. Gaididei, Topologically stable magnetization states on a spherical shell: Curvature-stabilized skyrmions, *Phys. Rev. B* **94**, 144402 (2016).
- [31] O. V. Pylypovskiy, D. Makarov, V. P. Kravchuk, Y. Gaididei, A. Saxena, and D. D. Sheka, Chiral Skyrmion and Skyrmionium States Engineered by the Gradient of Curvature, *Phys. Rev. Appl.* **10**, 064057 (2018).
- [32] V. P. Kravchuk, D. D. Sheka, A. Kákay, O. M. Volkov, U. K. Röbber, J. van den Brink, D. Makarov, and Y. Gaididei, Multiplet of Skyrmion States on a Curvilinear Defect: Reconfigurable Skyrmion Lattices, *Phys. Rev. Lett.* **120**, 067201 (2018).
- [33] V. P. Kravchuk, D. D. Sheka, U. K. Röbber, J. van den Brink, and Y. Gaididei, Spin eigenmodes of magnetic skyrmions and the problem of the effective skyrmion mass, *Phys. Rev. B* **97**, 064403 (2018).
- [34] A. Kákay, E. Westphal, and R. Hertel, Speedup of FEM micromagnetic simulations with graphical processing units, *IEEE Trans. Magn.* **46**, 2303 (2010).
- [35] K. V. Yershov, V. P. Kravchuk, D. D. Sheka, O. V. Pylypovskiy, D. Makarov, and Y. Gaididei, Geometry-induced motion of magnetic domain walls in curved nanostripes, *Phys. Rev. B* **98**, 060409(R) (2018).
- [36] K. V. Yershov, V. P. Kravchuk, D. D. Sheka, and Y. Gaididei, Curvature-induced domain wall pinning, *Phys. Rev. B* **92**, 104412 (2015).
- [37] H. Yang, A. Thiaville, S. Rohart, A. Fert, and M. Chshiev, Anatomy of Dzyaloshinskii–Moriya interaction at Co/Pt Interfaces, *Phys. Rev. Lett.* **115**, 267210 (2015).
- [38] S. Rohart and A. Thiaville, Skyrmion confinement in ultrathin film nanostructures in the presence of Dzyaloshinskii–Moriya interaction, *Phys. Rev. B* **88**, 184422 (2013).
- [39] G. Carbou, Thin layers in micromagnetism, *Mathematical Models and Methods in Applied Sciences (M3AS)* **11**, 1529 (2001).
- [40] G. D. Fratta, Dimension reduction for the micromagnetic energy functional on curved thin films, [arXiv:1609.08040](https://arxiv.org/abs/1609.08040).
- [41] G. D. Fratta, C. B. Muratov, F. N. Rybakov, and V. V. Slastikov, Variational principles of micromagnetics revisited, [arXiv:1905.04568](https://arxiv.org/abs/1905.04568).
- [42] These functions are interconnected by means of the relation $r'(s)^2 + z'(s)^2 \equiv 1$. The requirement that the surface is smooth at $s = 0$ imposes additional conditions on these functions: $z'(0) = 0$, $r(0) = 0$ and $r'(0) = 1$. While the requirement of localization of the curvilinear defect results in $z(s) \rightarrow 0$ and $r(s) \rightarrow s + \text{const.}$, when $s \rightarrow \infty$.

- [43] D. Cortes-Ortuno and P. Landeros, Influence of the Dzyaloshinskii-Moriya interaction on the spin-wave spectra of thin films, *J. Phys.: Condens. Matter* **25**, 156001 (2013).
- [44] Note that the Kittel mode has the same azimuthal symmetry as the CCW mode, namely $\mu = -1$. Also, the localization area of the eigenfunctions f and g of the CCW mode of the quasinormal state diverges in the limit $\mathcal{A} \rightarrow 0$ providing the transition to the Kittel mode with $f = g = \text{const}$.
- [45] B. Satywali, F. Ma, S. He, M. Raju, V. P. Kravchuk, M. Garst, A. Soumyanarayanan, and C. Panagopoulos, Gyrotropic resonance of individual Néel skyrmions in Ir/Fe/Co/Pt multilayers, [arXiv:1802.03979](https://arxiv.org/abs/1802.03979).
- [46] M. Mruczkiewicz, P. Gruszecki, M. Krawczyk, and K. Y. Guslienko, Azimuthal spin-wave excitations in magnetic nanodots over the soliton background: Vortex, bloch, and Néel-like skyrmions, *Phys. Rev. B* **97**, 064418 (2018).
- [47] F. G. Mertens and A. R. Bishop, Dynamics of vortices in two-dimensional magnets, in *Nonlinear Science at the Dawn of the 21th Century*, edited by P. L. Christiansen, M. P. Soerensen, and A. C. Scott, Lecture Notes in Physics Vol. 542 (Springer-Verlag, Berlin, 2000), pp. 137–170.
- [48] O. A. Tretiakov, D. Clarke, G.-W. Chern, Y. B. Bazaliy, and O. Tchernyshyov, Dynamics of Domain Walls in Magnetic Nanostrips, *Phys. Rev. Lett.* **100**, 127204 (2008).
- [49] Vectors \tilde{g}_i compose a basis in the tangent space.
- [50] Note that $(\mathbf{a} \otimes \mathbf{b})\mathbf{c} = \mathbf{a}(\mathbf{b} \cdot \mathbf{c})$.
- [51] One should use here the property $\varepsilon_{ikl}\varepsilon^{ikl} = 2\delta_i^j$.
- [52] Strictly speaking $X^3 \equiv \text{const}$. The choice $X^3 \equiv 0$ is convenient because in this case one can work only with the metric on the surface σ .
- [53] A. P. Malozemoff and J. C. Slonzewski, *Magnetic Domain Walls in Bubble Materials* (Academic, New York, 1979).
- [54] D. L. Huber, Equation of motion of a spin vortex in a two-dimensional planar magnet, *J. Appl. Phys.* **53**, 1899 (1982).
- [55] M. J. Bowick and L. Giomi, Two-dimensional matter: order, curvature and defects, *Adv. Phys.* **58**, 449 (2009).
- [56] A. Z. Petrov, *Einstein Spaces* (Pergamon, New York, 1969).
- [57] O. Veblen, Normal coordinates for the geometry of paths, *Proc. Natl. Acad. Sci.* **8**, 192 (1922).